JBC RESEARCH ARTICLE

A conserved residue in the P2X4 receptor has a nonconserved function in ATP recognition

Received for publication, September 15, 2020, and in revised form, April 5, 2021 Published, Papers in Press, April 23, 2021,
https://doi.org/10.1016/j.jbc.2021.100655

Ping-Fang Chen[1,‡], Xue-Fei Ma[2,3,‡], Liang-Fei Sun[1,‡], Yun Tian[3], Ying-Zhe Fan[4], Peiwang Li[5], Zhihong Xiao[5], Michael X. Zhu[6], Chang-Run Guo[2], Changzhu Li (李昌珠)[5,*], Ye Yu (于烨)[1,2,7,*], and Jin Wang (汪津)[2,*]

From the [1]Department of Pharmacology and Chemical Biology, Institute of Medical Sciences, Shanghai Jiao Tong University School of Medicine, Shanghai, China; [2]School of Basic Medicine and Clinical Pharmacy, China Pharmaceutical University, Nanjing, China; [3]College of Bioscience and Biotechnology, Hunan Agricultural University, Changsha, China; [4]Putuo Hospital, Shanghai University of Chinese Traditional Medicine, Shanghai, China; [5]State Key Laboratory of Utilization of Woody Oil Resource, Hunan Academy of Forestry, Changsha, China; [6]Department of Integrative Biology and Pharmacology, McGovern Medical School, The University of Texas Health Science Center at Houston, Houston, Texas, USA; [7]State Key Laboratory for Chemistry and Molecular Engineering of Medicinal Resources, Collaborative Innovation Center for Guangxi Ethnic Medicine, School of Chemistry and Pharmaceutical Sciences, Guangxi Normal University, Guilin, China

Edited by Roger Colbran

Highly conserved amino acids are generally anticipated to have similar functions across a protein superfamily, including that of the P2X ion channels, which are gated by extracellular ATP. However, whether and how these functions are conserved becomes less clear when neighboring amino acids are not conserved. Here, we investigate one such case, focused on the highly conserved residue from P2X4, E118 (rat P2X4 numbering, rP2X4), a P2X subtype associated with human neuropathic pain. When we compared the crystal structures of P2X4 with those of other P2X subtypes, including P2X3, P2X7, and AmP2X, we observed a slightly altered side-chain orientation of E118. We used protein chimeras, double-mutant cycle analysis, and molecular modeling to reveal that E118 forms specific contacts with amino acids in the "beak" region, which facilitates ATP binding to rP2X4. These contacts are not present in other subtypes because of sequence variance in the beak region, resulting in decoupling of this conserved residue from ATP recognition and/or channel gating of P2X receptors. Our study provides an example of a conserved residue with a specific role in functional proteins enabled by adjacent nonconserved residues. The unique role established by the E118-beak region contact provides a blueprint for the development of subtype-specific inhibitors of P2X4.

The side-chain orientation of a given residue is closely related to protein functions such as ligand recognition (1) and conformational transitions (2) of these proteins during allosteric processes. Fine interpretation of the relationship between residue function and side-chain orientation at atomic level will advance our understanding of protein function (3) and provide more accurate structural information for future drug design (4, 5). In general, the relationship between 3D structural information and function is more conserved in a protein superfamily than that of primary amino acid sequence (6, 7). And it has also been suggested that in a given functional protein superfamily, conserved amino acids have similar functions among different members (8, 9). However, if there are nonconserved residues located around the highly conserved residues, how do these surrounding residues affect the function of those conserved residues? Do the conserved and nonconserved residues encode different structural information together? Although there has been a great deal of studies aimed at understanding how do primary sequences determine the 3D structure and function of proteins, studying the relationship between sequence, structure, and function (RSSF) remains a daunting task. However, in recent years, a number of different crystal or cryo-EM structures have been identified (10–12), including structures from different subtypes and species, or at different states (*apo* or open states), such as the P2X receptors (13–21), providing invaluable information used to study the RSSF of a particular protein superfamily.

P2X receptors are ligand-gated ion channels activated by extracellular ATP, and seven different subtypes (P2X1–7) have been cloned in recent years (22). These different P2X receptors are implicated in different physiological processes, such as synaptic transmission (23), pain sensation (24–26), and immune and cardiovascular regulations (27, 28). Therefore, P2X receptors are considered as potential therapeutic targets for neuropathic pain, inflammation, rheumatoid arthritis, chronic cough, and others (29–31). Prior to the first determination of the crystal structure of P2X receptors, studies on the structure and function relationship of these receptors focused on various conserved residues and their role in ATP recognition, channel pore location, and others (32–35). In the past decade, crystal or cryo-EM structures of several P2X receptors were determined, including crystal structures of zebrafish (*Danio rerio*) P2X4 (zfP2X4) (13–15), gulf coast tick (*Amblyomma maculatum*) P2X (AmP2X) (16), chicken (*Gallus gallus*

‡ Equal contributions to this work.
* For correspondence: Jin Wang, wangjin@cpu.edu.cn; Ye Yu, yuye@shsmu.edu.cn; Changzhu Li, lichangzhu2013@aliyun.com.

domesticus) P2X7 (ckP2X7) (17), giant panda (*Ailuropoda melanoleuca*) P2X7 (pdP2X7) (21), human (*Homo sapiens*) P2X3 (hP2X3) (18, 19), and cryo-EM structures of rat (*Rattus norvegicus*) P2X7 (rP2X7) (20) in the closed/open/desensitized/antagonist-bound states. Thus, the study of P2X RSSF has entered a poststructure era where we can more accurately re-evaluate the structure and function relationship of P2X receptors.

In this study, we compared the conformation/side-chain orientation of some conserved residues in several recently structurally identified P2X subtypes and found that a highly conserved residue E121 (equal to E118 in rP2X4) in the head domain of zfP2X4 has a different side-chain orientation from the other subtypes. Through a combination of molecular dynamics (MD) simulations, chimera construction, mutagenesis, and electrophysiological studies, we suggest that the unique side-chain orientation of E121 provides additional contacts between this residue and amino acids in the beak region, thus establishing a special role in determining the apparent affinity of ATP in rP2X4 but not in other P2X subtypes.

Results

E121 is a highly conserved residue in zfP2X4 with a different side-chain orientation compared with other P2X subtypes

To reassess the role of conserved residues in P2X channel function, we compared the side-chain orientations of all conserved residues in several P2X subtypes whose 3D structures have been determined by X-ray crystallography, including zfP2X4 (Protein Data Bank [PDB] IDs: 4DW0 and 4DW1), hP2X3 (PDB IDs: 5SVJ and 5SVK), AmP2X (PDB ID: 5F1C), ckP2X7 (PDB ID: 5XW6), and pdP2X7 (PDB ID: 5U1L). The cryo-EM structures of rP2X7 were not included into this comprehensive comparison since we could not exclude possible influence of two different methods (single-particle cryo-EM and X-ray crystallography) in determining residue side-chain orientation. Through a comprehensive structural superimposition, we found that three highly conserved residues R298, K316, and E121 (zfP2X4 numbering) have different side-chain orientations in different P2X subtypes (Table 1). R298 and K316 produce direct contacts with the agonist ATP in the open structure of zfP2X4 (Fig. 1*A*), and it is therefore reasonable to infer that the different side-chain orientation of these two residues may contribute to distinct recognition patterns for free ATP^{4-} or $MgATP^{2-}$ and/or distinct ATP affinities in various P2X subtypes (36). E121 is located far away from the ATP-binding site in the head domain of zfP2X4 (Fig. 1, *A* and *B*), and its role in the channel function of the P2X receptors remains unclear.

The dihedral angle $\chi_{C\alpha-C\beta-C\gamma-C\delta}$ of E121 in zfP2X4 at the resting (PDB ID: 4DW0) and open (PDB ID: 4DW1) states was 166.1° and −174.4°, respectively (Fig. 1*B*), showing extended conformations. In other P2X isoforms, such as hP2X3 in the resting (PDB ID: 5SVJ) and open states (PDB ID: 5SVK), and ckP2X7 with an incorporation of competitive inhibitor 2′,3′-O-(2,4,6-trinitrophenyl) adenosine 5′-triphosphate (PDB ID: 5XW6), the $\chi_{C\alpha-C\beta-C\gamma-C\delta}$ of identical residues ranged from 60° to −80° (Fig. 1, *D–F*) for a bent conformation (Fig. 1, *D–F*). The side chain of the equivalent residue of pdP2X7 was shortened (D121; Fig. 1, *C* and *G*), so we could not measure the dihedral angle of this residue. The recent determined cryo-EM structures of rP2X7 reveal the extended conformation of the same residue E121 at the resting state ($\chi_{C\alpha-C\beta-C\gamma-C\delta}$ = 172.9°) and the bent conformation at the open state ($\chi_{C\alpha-C\beta-C\gamma-C\delta}$ = −55.2°) (Fig. 1*H*).

To test whether the conformation of E121 in zfP2X4 and equivalent residues in other P2X subtypes are stable in a physiological condition, a series of 0.5-μs MD simulations were performed on aforementioned crystal or cryo-EM structures. These simulations showed that during simulations of zfP2X4, E121 always maintained an extended conformation ($\chi_{C\alpha-C\beta-C\gamma-C\delta}$ = 180° or −180°) both in the resting and open states, whereas the same residues in other structures remained in the bent conformation ($\chi_{C\alpha-C\beta-C\gamma-C\delta}$ = ∼60°–80°) (Fig. 2). The $\chi_{C\alpha-C\beta-C\gamma-C\delta}$ of E121 also remained at ±180° and ∼60 to 80° when MD simulations were performed based on cryo-EM structures of rP2X7 at the resting and open states, respectively, indicating that the MD simulation did not change the initial $\chi_{C\alpha-C\beta-C\gamma-C\delta}$ of E121 of rP2X7 (Fig. 1*H*). Thus, the side-chain orientation of these equivalent residues is not a transient "snapshot" in the structure determination but is also relatively stable in the structure fluctuations.

Alanine substitutions of E121 in zfP2X4 and E118 in rP2X4 significantly alter the apparent affinity of ATP

Mutagenesis performed in these residues showed that $zfP2X4^{E121A}$ resulted in an approximately 15-fold increase

Table 1
The side-chain dihedral angles of a few residues in various crystal structures of P2X receptors

	zfP2X4		hP2X3		AmP2X	pdP2X	ckP2X7
Dihedral angles	Resting (PDB ID: 4DW0)	Open (PDB ID: 4DW1)	Resting (PDB ID: 5SVJ)	Open (PDB ID: 5SVK)	Open (PDB ID: 5F1C)	Resting (PDB ID: 5U1L)	Inhibition (PDB ID: 5XW6)
$C_\alpha-C_\beta-C_\gamma-C_\delta$	E121		E109		E129	D121	E109
	166.1	−171.4	75.2	−76.6	−73.2	—	63.3
	R298		R281		R313	R294	R280
$C_\alpha-C_\beta-C_\gamma-C_\delta$	176.5	171.7	178.6	172.5	−177.1	174.3	−179.3
$C_\beta-C_\gamma-C_\delta-N_\beta$	−87.8	99.1	171.2	101.9	−174.4	61	76.8
$C_\gamma-C_\delta-N_\beta-C_\varepsilon$	−86.5	113.1	89.8	107.0	87.6	108.3	105.8
	K316		K299		K327	K311	K298
$C_\alpha-C_\beta-C_\gamma-C_\delta$	−166.4	173.8	−176.5	163.1	−172.9	−169.7	162.2
$C_\beta-C_\gamma-C_\delta-C_\varepsilon$	−177.6	175.8	−173.9	177.4	−176.7	−52.4	−160.9

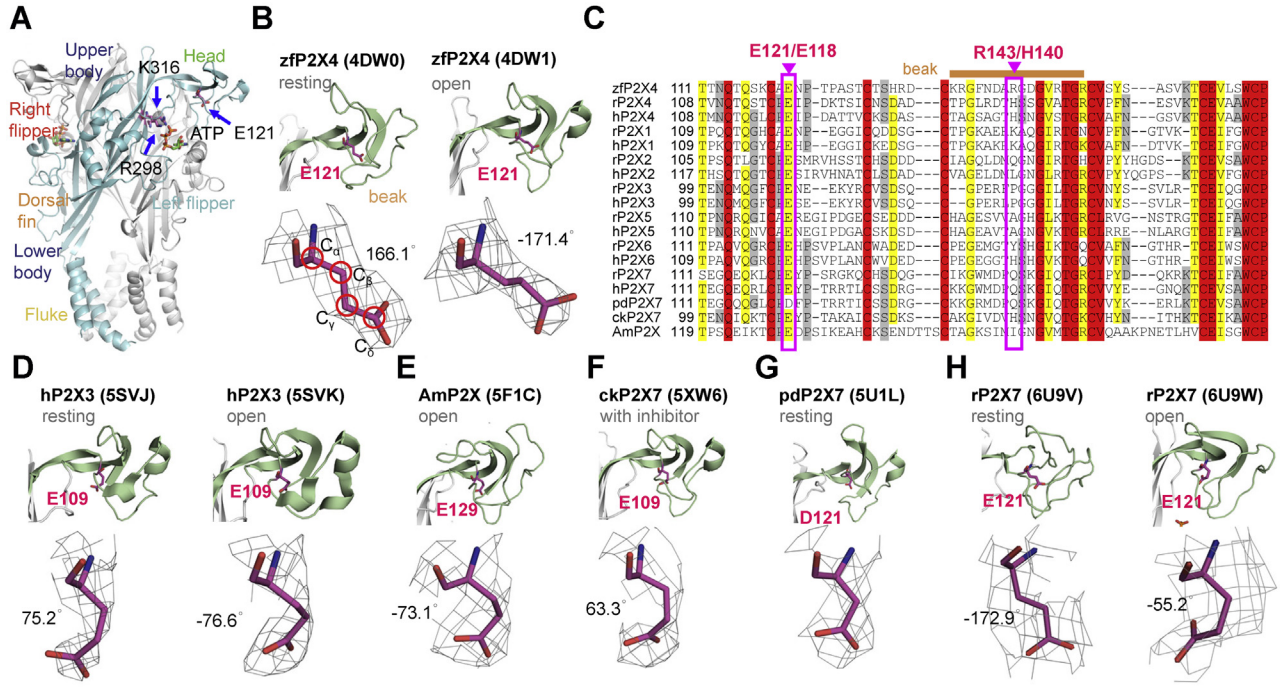

Figure 1. Side-chain orientations of E121 in zfP2X4 and equivalent residues in other P2X receptors. *A*, residues E121, R298, and K313 highlighted in the open structure of zfP2X4 (Protein data Bank [PBD] ID: 4DW1). The different domains are named head, dorsal fin (DF), left flipper (LF), right flipper (RF), body and fluke, respectively. *B*, zoom-in view of the location of E121 (*upper*) and 2Fo–Fc omit map for E121 (*lower*) in zfP2X4 at the resting (PDB ID: 4DW0, *left*) and open (*right*) states. *Red circles* indicate the atoms chosen to define the dihedral angle $\chi_{C\alpha-C\beta-C\gamma-C\delta}$. *C*, the sequence alignment of the head domain in P2X family. *Pink boxed regions* highlight the highly conserved residue E121/E118 and nonconserved residue R143/H140 (zfP2X4/rP2X4 numbering) in P2X receptors. *Sand bar* indicates residues in the beak region. *D–G*, side-chain orientations of E109 in the apo (PDB ID: 5SVJ) and open (PDB ID: 5SVK) crystal structures of hP2X3, E129 in the open structure of AmP2X (PDB ID: 5F1C) (*E*), E109 in the crystal structure of ckP2X7 in complex with inhibitor (PDB ID: 5XW6) (*F*) and D121 in the apo crystal structure of pdP2X7 (PDB ID: 5U1L) (*G*). *H*, the side-chain orientation of E121 in the cryo-EM structure of rP2X7 at the resting (PDB ID: 6U9V) and open (PDB ID: 6U9W) states. rP2X4, rat (*Rattus norvegicus*) P2X4; zfP2X4, zebrafish (*Danio rerio*) P2X4.

in the apparent affinity of ATP (concentration yielding half-maximal activation, EC_{50} = 1426 ± 733 and 89.6 ± 18.1 μM for zfP2X4^{WT} and zfP2X4^{E121A}, respectively, $p < 0.05$; Fig. 3*A*), and other subtypes of corresponding mutations did not or slightly change the apparent affinity of ATP (EC_{50} = 0.45 ± 0.07 and 0.58 ± 0.07 μM for hP2X3^{WT} and hP2X3^{E109A}, respectively, Fig. 3*C*; 43.5 ± 4.7 and 32.9 ± 4.2 μM for AmP2X^{WT} and AmP2X^{E129A}, respectively, Fig. 3*D*; 4.77 ± 0.69

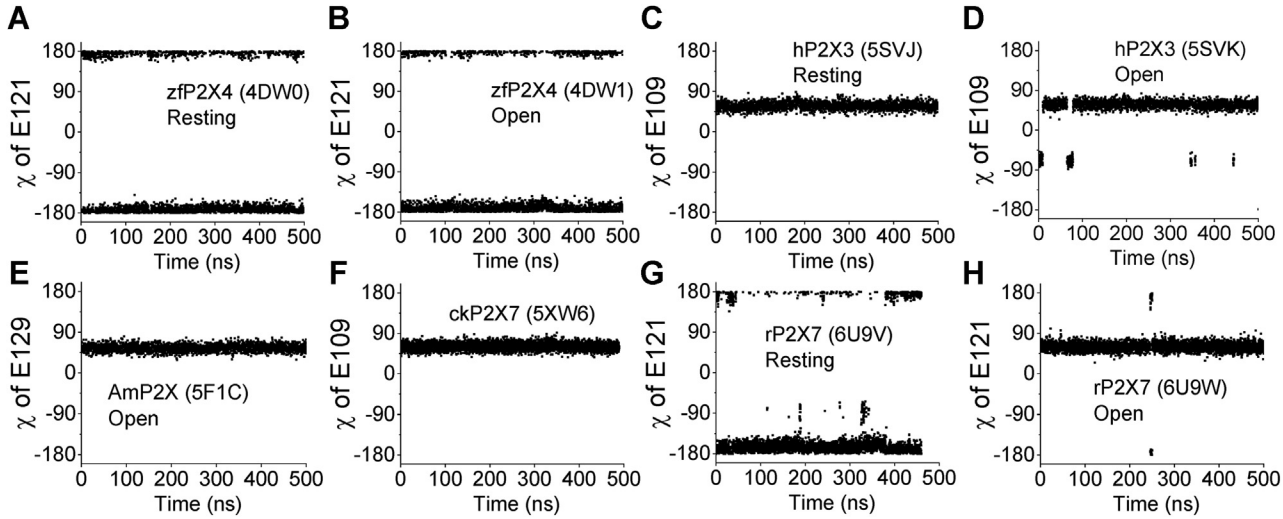

Figure 2. Molecular dynamics (MD) simulations used to test the stability of dihedral angle $\chi_{C\alpha-C\beta-C\gamma-C\delta}$ in various P2X structures. *A–H*, the fluctuation of dihedral angle $\chi_{C\alpha-C\beta-C\gamma-C\delta}$ during 0.5-μs MD simulations of zfP2X4 (*A*, resting; *B*, open), hP2X3 (*C*, resting; *D*, open), AmP2X (*E*, open), ckP2X7 (*F*, with bound inhibitor), and rP2X7 (*G*, resting; *H*, open). The trajectories were sampled every 200 ps. AmP2X, gulf coast tick (*Amblyomma maculatum*) P2X; ckP2X7, chicken (*Gallus gallus domesticus*) P2X7; hP2X3, human (*Homo sapiens*) P2X3; rP2X7, rat (*Rattus norvegicus*) P2X7; zfP2X4, zebrafish (*Danio rerio*) P2X4.

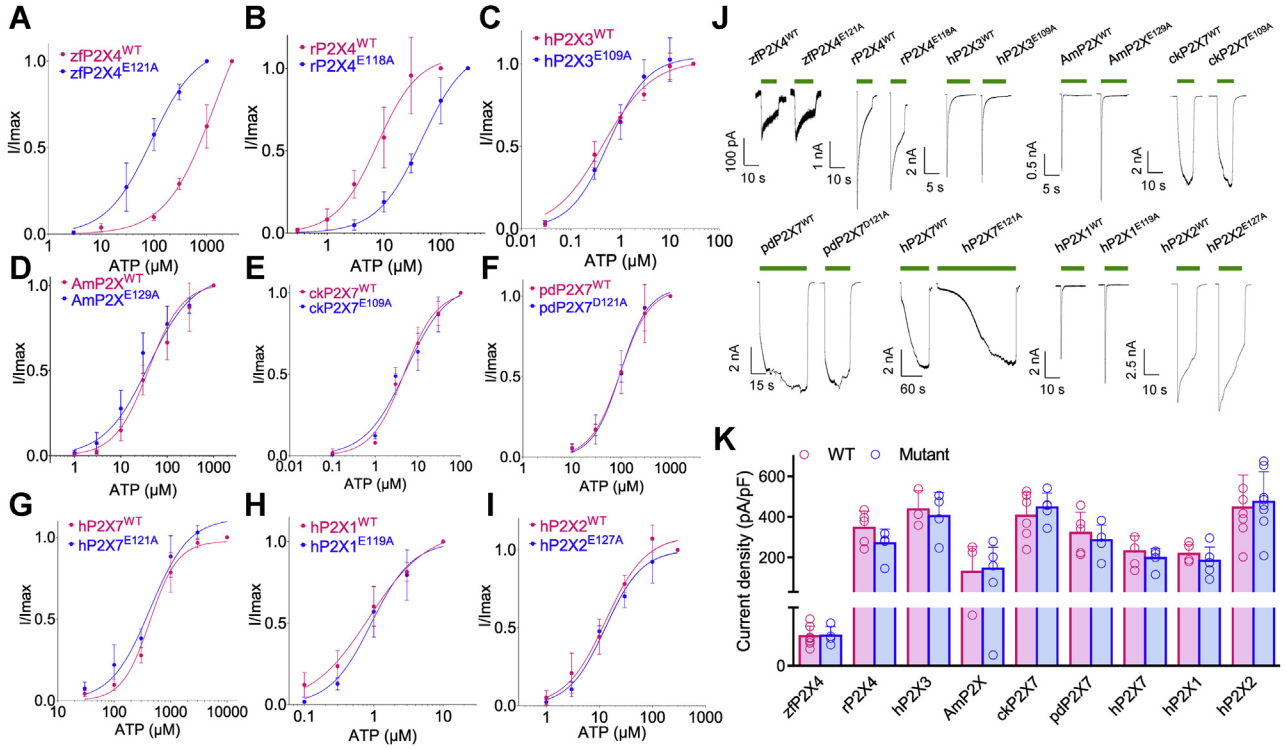

Figure 3. Altered apparent ATP affinities of ATP in P2X mutants. *A–I*, concentration–response curves of ATP in WT and equivalent alanine substitutions in zfP2X4 (*A*), rP2X4 (*B*), hP2X3 (*C*), AmP2X (*D*), ckP2X7 (*E*), pdP2X7 (*F*), hP2X7 (*G*), hP2X1 (*H*), and hP2X2 (*I*). The *solid lines* are fitted by Hill equation (mean ± SD, n = 3–7, EC_{50} = 1426 ± 733 and 89.6 ± 18.1 μM, n_H = 0.94 ± 0.16 and 1.02 ± 0.18 for $zfP2X4^{WT}$ and $zfP2X4^{E121A}$; EC_{50} = 7.65 ± 1.56 and 45.92 ± 9.05 μM, n_H = 1.20 ± 0.22 and 1.11 ± 0.15 for $rP2X4^{WT}$ and $rP2X4^{E118A}$; EC_{50} = 0.45 ± 0.07 and 0.58 ± 0.07 μM, n_H = 0.94 ± 0.16 and 1.02 ± 0.18 for $hP2X3^{WT}$ and $hP2X3^{E109A}$; EC_{50} = 43.5 ± 4.7 and 32.9 ± 4.2 μM, n_H = 1.14 ± 0.11 and 0.99 ± 0.09 for $AmP2X^{WT}$ and $AmP2X^{E129A}$; EC_{50} = 4.77 ± 0.69 and 5.31 ± 1.26 μM, n_H = 1.14 ± 0.16 and 0.91 ± 0.16 for $ckP2X7^{WT}$ and $ckP2X7^{E109A}$; EC_{50} = 95.7 ± 17.6 and 96.6 ± 10.9 μM, n_H = 1.44 ± 0.32 and 1.53 ± 0.24 for $pdP2X7^{WT}$ and $pdP2X7^{D121A}$; EC_{50} = 496.7 ± 44.2 and 360.5 ± 54.3 μM, n_H = 1.71 ± 0.19 and 1.34 ± 0.20 for $hP2X7^{WT}$ and $hP2X7^{E121A}$; EC_{50} = 0.86 ± 0.16 and 0.92 ± 0.17 μM, n_H = 1.04 ± 0.16 and 1.46 ± 0.33 for $hP2X1^{WT}$ and $hP2X1^{E119A}$; EC_{50} = 13.16 ± 1.97 and 12.92 ± 1.68 μM, n_H = 1.15 ± 0.17 and 1.26 ± 0.15 for $hP2X2^{WT}$ and $hP2X2^{E127A}$, respectively). I_{max} was defined as the saturating ATP-induced current for WT and equivalent alanine-substituted P2X receptors, except for the maximum concentration of ATP (3 mM) used for $zfP2X4^{E121A}$. *J* and *K*, representative current traces (*J*) and pooled data (*K*) for WT and equivalent alanine substitution of P2X receptors. The scatter of each *open circle* represents each measurement, n = 7, 4, 5, 5, 3, 4, 4, 5, 6, 5, 5, 5, 5, 5, 5, 6, 8, and 8, from *left* to *right*, respectively. AmP2X, gulf coast tick (*Amblyomma maculatum*) P2X; ckP2X7, chicken (*Gallus gallus domesticus*) P2X7; hP2X3, human (*Homo sapiens*) P2X3; pdP2X7, giant panda (*Ailuropoda melanoleuca*) P2X7; rP2X4, rat (*Rattus norvegicus*) P2X4; zfP2X4, zebrafish (*Danio rerio*) P2X4.

and 5.31 ± 1.26 μM for $ckP2X7^{WT}$ and $ckP2X7^{E109A}$, respectively, Fig. 3*E*; 95.7 ± 17.6 and 96.6 ± 10.9 μM for $pdP2X7^{WT}$ and $pdP2X7^{D121A}$, respectively, Fig. 3*F*; 496.7 ± 44.2 and 360.5 ± 54.3 μM for $hP2X7^{WT}$ and $hP2X7^{E121A}$, measured in Ca^{2+}-/Mg^{2+}-free solutions, Fig. 3*G*; $p > 0.05$). Notably, the ATP-induced maximum currents were not affected by these alanine substitutions (Fig. 3, *J* and *K*). These results suggest that the unique side-chain orientation of E121 in the zfP2X4 receptor has a special role in determining the apparent affinity for ATP.

The underlying mechanism of the altered apparent ATP affinity in $zfP2X4^{E121A}$ should be further investigated; however, previous studies have shown that zfP2X4 is poorly expressed in mammalian cells and insensitive to extracellular ATP (EC_{50} > 1 mM) (13, 14), making it difficult to study the mechanism by using comprehensive mutagenesis together with electrophysiological recordings. Therefore, the following chimera constructions, double-mutant cycle analysis, and interaction–function correlation analysis were carried out in rP2X4 rather than zfP2X4 receptors. In addition, to obtain more accurate information for rP2X4 studies, we built homology models of rP2X4 and performed MD simulations of rP2X4 WT and its mutants.

Similarly, alanine substitution on the equivalent residue E118A of rP2X4 significantly changed the apparent ATP affinity of rP2X4 (7.65 ± 1.56 and 45.9 ± 9.1 μM for $rP2X4^{WT}$ and $rP2X4^{E118A}$, $p < 0.05$, respectively; Fig. 3*B*). As controls, the corresponding mutants in hP2X1 and hP2X2 had no effect on the apparent affinity of ATP (EC_{50} = 0.86 ± 0.16 and 0.92 ± 0.17 μM for $hP2X1^{WT}$ and $hP2X1^{E119A}$, $p > 0.05$; EC_{50} = 13.16 ± 1.97 and 12.92 ± 1.67 μM for $hP2X2^{WT}$ and $hP2X2^{E127A}$, $p > 0.05$; Fig. 3, *H* and *I*). Only negligible ATP current could be detected in cells expressing homomeric mammalian P2X5 and P2X6 receptors, and therefore, effects of the same mutants on these two P2X subtypes were not measured. Thus, the apparent affinity of ATP was only affected by the substitution of alanine in E118 or E121 in P2X4, but not in all other P2X receptor subtypes tested, although this glutamate is highly conserved.

Additional mutants in E118 were constructed, and their effects on the affinity of rP2X4 were measured by a sequential ATP application protocol. The ratio (*R*) of currents ($I_{1\ mM}/I_{8\ \mu M}$) induced by 8 μM (EC_{50}) and 1 mM (saturated) ATP was used to simplify the effect of various mutants on the apparent affinity of rP2X4 (Fig. 4*A*). rP2X4 WT had an *R* value of 2.16 ± 0.22, with

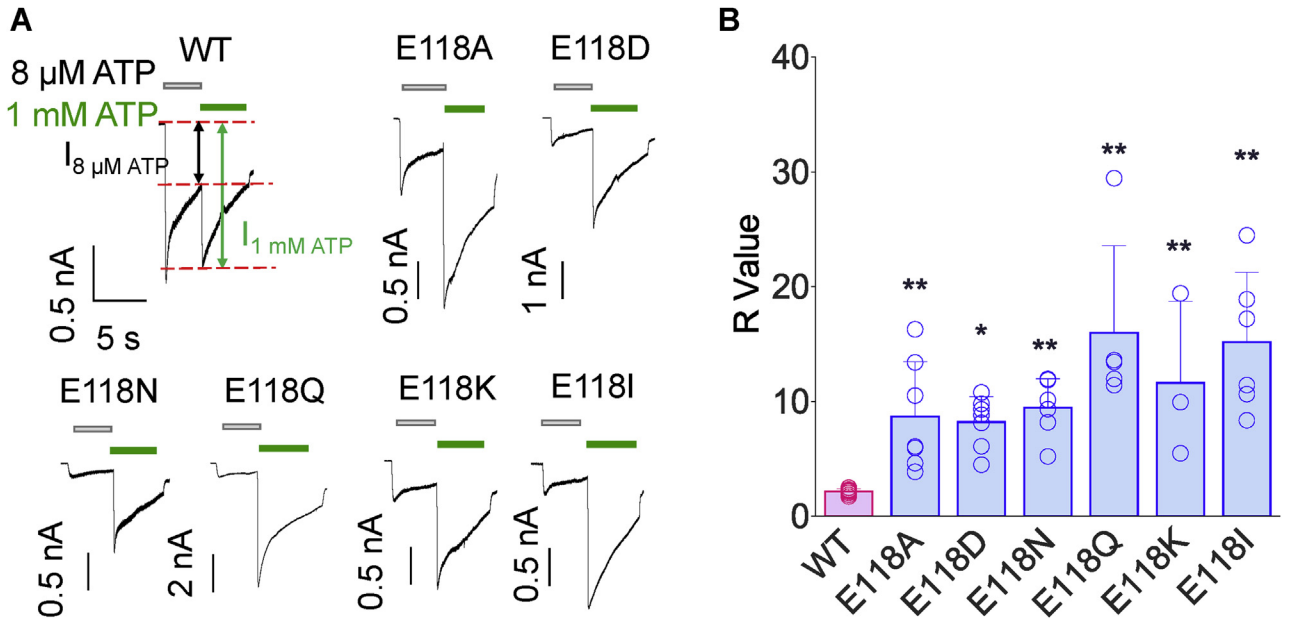

Figure 4. Role of E118 in determining the apparent affinity of rP2X4. *A* and *B*, representative current traces (*A*) and pooled data (*B*) for WT and rP2X4 mutants. About 8 μM ATP was first applied (*gray bars*) and then switched to 1 mM ATP (*green bars*). *R* values are derived from the ratio of 1 mM ATP-induced current to 8 μM ATP-induced current. *Open circles* of each scatter represent each measurement through whole-cell recordings, n = 15, 7, 7, 6, 5, 3, and 6, from *left* to *right*, respectively. *$p < 0.05$, **$p < 0.01$ *versus* WT, one-way ANOVA with Bonferroni post-test ($F(6, 42) = 11.54$, $p < 0.0001$). rP2X4, rat (*Rattus norvegicus*) P2X4.

higher *R* values indicating higher EC_{50} values for the mutants (Fig. 4, *A* and *B*). Any small change in the polarity or size at position 118 significantly impaired the apparent ATP sensitivity of rP2X4, for example, by replacing the Glu by Asp ($I_{1\ mM}/I_{8\ \mu M}$ = 8.20 ± 2.20), Lys (11.61 ± 7.12), Ile (15.16 ± 6.09), Asn (9.44 ± 2.54), and Gln (15.98 ± 7.60). These results imply that E118 exerts its role through a strict interaction with adjacent residues.

The sequence differences of the beak region result in higher and lower EC_{50} values for zfP2X4^{E121A} and rP2X4^{E118A} compared with WT channels, respectively

Although zfP2X4^{E121A} and rP2X4^{E118A} could significantly change the apparent affinity of ATP, zfP2X4^{E121A} decreased, whereas rP2X4^{E118A} increased the EC_{50} values of ATP. This difference should be further addressed. Chimeras zfP2X4$^{r\text{-}beak}$ (with residues 136–148 replacements, zfP2X4 numbering) and rP2X4$^{zf\text{-}beak}$ (with residues 133–145 replacements, rP2X4 numbering) were built by swapping their beak region sequences (Fig. 5, *A* and *B*). The zfP2X4$^{r\text{-}beak}$ chimera led ∼10-fold increases in the apparent affinity of ATP (EC_{50} = 121.9 ± 11.5 μM and 1.43 ± 0.73 mM for zfP2X4$^{r\text{-}beak}$ and WT, respectively; Fig. 5*C*). As control, the rP2X4$^{zf\text{-}beak}$ chimera resulted in an approximately 40-fold decrease in the apparent affinity of ATP (EC_{50} = 232.3 ± 50.3 and 7.65 ± 1.56 μM for rP2X4$^{zf\text{-}beak}$ and WT, respectively; Fig. 5*D*). However, there was no significant difference in ATP-induced maximum currents between WT and rP2X4 mutants (Fig. 5*E*). These two chimeras indicated that the sequence of the beak region correlates well with the apparent affinity of ATP in P2X4 receptors.

Interestingly, alanine substitution at the Glu residue identical to E121 in the chimera zfP2X4$^{r\text{-}beak}$ (zfP2X4$^{E121A/r\text{-}beak}$) significantly increased the EC_{50} of ATP from 0.12 to over 1 mM (Fig. 5*C*). However, the EC_{50} of rP2X4$^{E118A/zf\text{-}beak}$ (161.7 ± 26.5 μM) did not change compared with rP2X4$^{zf\text{-}beak}$ (232.3 ± 50.3 μM) ($p > 0.05$; Fig. 5*D*). In addition, double-mutant cycle analysis indicated that E118 correlates with the introduced new beak region sequences ($\Delta\Delta G$ = −1.25 kcal/mol for rP2X4^{E118A}, rP2X4$^{zf\text{-}beak}$, and rP2X4$^{E118A/zf\text{-}beak}$; Fig. 5*F*), indicating strong interaction between the identical residue and introduced new beak regions in chimera channels (>0.35 kcal/mol) (37). Although the rP2X4$^{zf\text{-}beak}$-based E118A mutant has no influence on the EC_{50} of ATP, it is still reasonable to infer that sequences in the beak region are implicated in E118/E121-mediated ATP recognition of P2X4 receptors.

The role of E118 in the apparent affinity is associated with S141 and S142, two nonconserved amino acids in the beak region of rP2X4

We further studied how E118, together with the adjacent beak region, determines the apparent ATP affinity of rP2X4. During MD simulations of *apo* P2X receptors, the head domain behaves with a tendency to spontaneously move downward and a closure of ATP-binding site jaw, at least for P2X2, P2X3, and P2X4 (38–43). Here, rP2X4^{E118A} also exhibits similar head domain movement during MD simulations (Fig. 6*A*), indicating that E118A does not compromise the inherent dynamics of the head domain.

We then explored the possibility that polar contacts between E118 and adjacent residues may contribute the role of E118 in ATP recognition of P2X4 receptors. At the resting state, the polar residues within 5 Å of E118 are S124 and D138 (Fig. 6*B*). The alanine substitution of these two residues had no

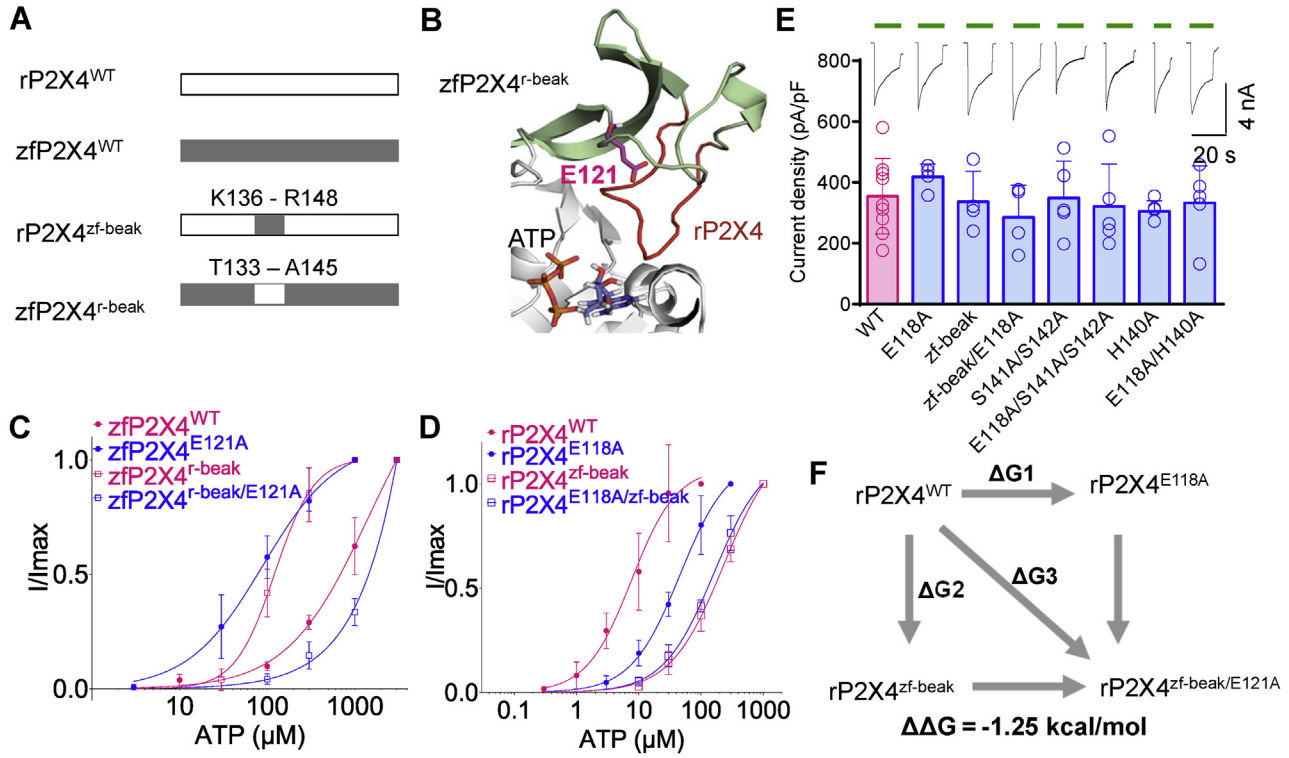

Figure 5. The role of E118 in the apparent affinity of ATP correlates with the sequence of the beak region in rP2X4. *A*, chimera construction of rP2X4 and zfP2X4. *B*, zoom-in view of the head and beak regions of the chimera zfP2X4$^{r\text{-}beak}$ (homology model). The beak region of zfP2X4 (*pale green*) is replaced by equivalent residues of rP2X4 (*red*). *C* and *D*, concentration–response curves of ATP in zfP2X4 WT and mutant receptors (*C*) and rP2X4 WT and mutant receptors (*D*). The *solid lines* are fitted by Hill equation (mean ± SEM, n = 3–6, EC_{50} = 232.3 ± 50.3 and 161.7 ± 26.5 μM, n_H = 1.02 ± 0.11 and 1.07 ± 0.11 for rP2X4$^{zf\text{-}beak}$ and rP2X4$^{zf\text{-}beak/E118A}$, respectively). The data of zfP2X4^{WT}, zfP2X4^{E121A}, rP2X4^{WT}, and rP2X4^{E118A} are the same as those shown in Figure 3, *A* and *B* and are shown here as controls. *E*, representative current traces and pooled data for rP2X4 WT and mutant receptors. The scatter of each *open circle* represents each measurement, n = 9, 4, 4, 4, 5, 5, 5, and 5, from *left* to *right*, respectively. One-way ANOVA with Bonferroni post-test ($F(7, 33) = 0.5623$; $p = 0.7807$). *F*, double-mutant cycle between E118 and the beak region of rP2X4. rP2X4, rat (*Rattus norvegicus*) P2X4; zfP2X4, zebrafish (*Danio rerio*) P2X4.

significant effect on *R* value of rP2X4 (Fig. 6*F*). At the open state, polar residues within 5 Å are S124 and S141 (Fig. 6*C*). In 0.5-μs MD simulations, we could observe stable hydrogen bond (H-bond) contacts between E118 and S141/S142 (Fig. 6*D*). The fact that S141A/S142A, as well as E118A/S141A/S142A, led to significantly changed *R* values of rP2X4 ($I_{1\ mM}/I_{8\ \mu M}$ = 9.10 ± 5.13 and 7.93 ± 2.03 for S141A/S142A and E118A/S141A/S142A, respectively; Fig. 6*F*) suggested that the E118 … S141/S142 interaction observed at the open state is essential for the apparent affinity of ATP in rP2X4 receptors.

Further double-mutant cycle analysis was performed to quantify these interactions. S141A/S142A, E118A, and E118A/S141A/S142A resulted in right shifts of dose-dependent response curves of ATP (EC_{50} = 7.65 ± 1.56, 51.50 ± 16.14, 45.92 ± 9.05, and 59.61 ± 13.22 μM for WT, S141A/S142A, E118A, and E118A/S141A/S142A, respectively; Fig. 6*G*). Accordingly, the free energy alterations were calculated to be 1.04, 1.11, and 1.20 kcal/mol for E118A, S141A/S142A, and E118A/S141A/S142A, respectively (Fig. 6*H*). The coupling energy $\Delta\Delta G$ of E118 and S141/S142 was −0.96 kcal/mol, which confirms the strong interaction between E118 and S141/S142 cluster (Fig. 6*H*).

In addition, we introduced tryptophan into the V161, a residue located near the E118 and S141/S142. Because V161 is located in the rigid β-sheet (β7) of the head domain, V161W will certainly block the S141/S142 … E118 interactions during channel opening of rP2X4 (Fig. 6*E*). Indeed, the *R* value of V161W increased to 13.7 ± 2.4 (Fig. 6*F*), indicating a significant decrease in the apparent affinity of ATP in rP2X4.

H140 mediates the correlation of E118 with ATP recognition of rP2X4

H140 is located in the lower beak region and may be involved in ATP recognition and channel gating of rP2X4 (Fig. 7*A*; *right*) (14, 15). During 0.5-μs MD simulations of rP2X4 WT with bound ATP, a tightening of the cleft between the dorsal fin and the rostral/head region and a shortening of the distance between ATP and H140 can be observed (Fig. 7*B*). In contrast, A118 swinged upward with H140 together and away from the bound ATP during MD simulations of rP2X4^{E118A} (Fig. 7, *C*–*E*). This altered allostery will unwind the interaction between ATP and H140 and the subsequent coordinated movement of the beak and dorsal fin domains, ultimately affecting the ATP recognition and channel gating of P2X4.

Double-mutant cycle analysis was also applied to confirm the coupling between E118 and H140. Single mutations E118A and H140A and double-mutant E118A/H140A resulted in increased EC_{50} values of ATP to 45.9 ± 9.1, 53.3 ± 9.1, and 55.1 ± 14.4 μM, respectively (Fig. 7*F*). The coupling free energy

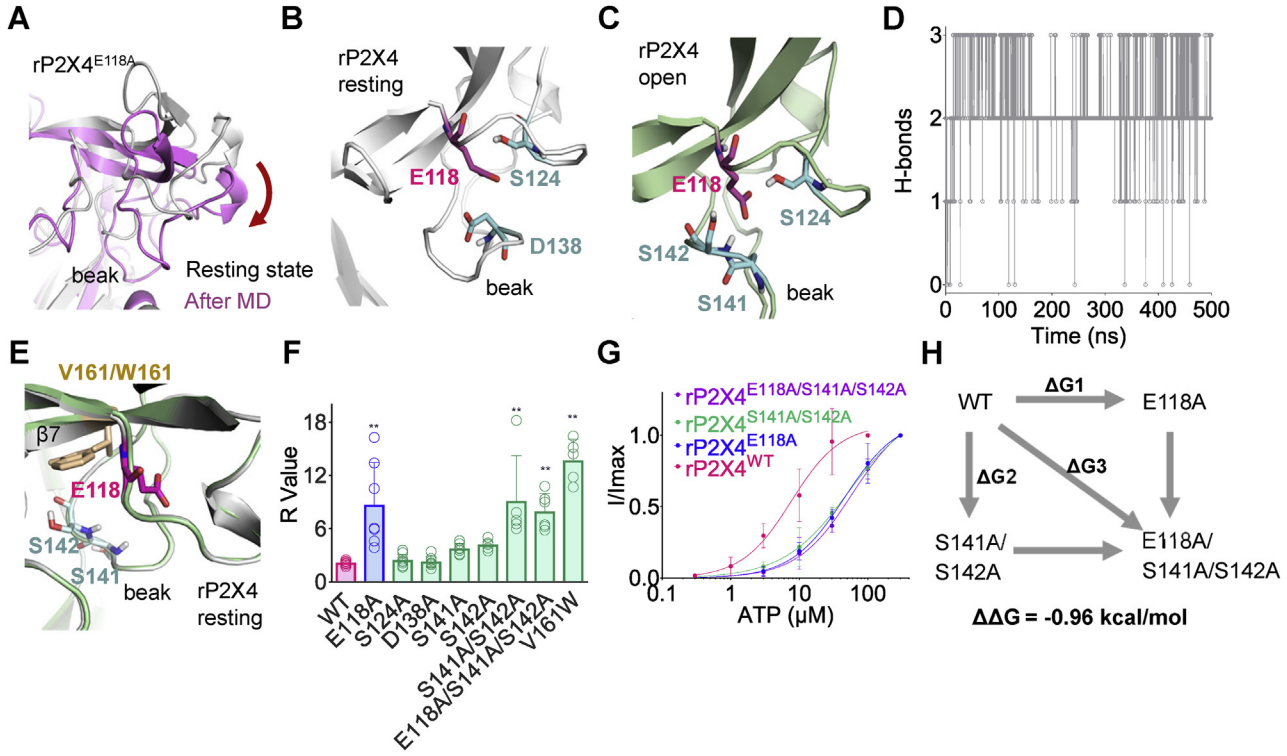

Figure 6. E118 interacts with S141/S142 in the beak region of rP2X4 receptors. *A*, downward motion of the head domain during 0.5-μs molecular dynamics (MD) simulation of rP2X4^{E118A} in the resting state. *B*, polar amino acids of the head domain near E118 (within 5 Å) in rP2X4 in the resting (*B*) and open (*C*) states. *D*, the H-bond interactions between E118 and S141/S142 during 0.5-μs MD simulation of open structure of rP2X4. The trajectory was sampled every 200 ps. *E*, superimposed homology models of V161 and its tryptophan substitution (W161) to show the position of this residue (at rigid β7) near to S141, S142, and E118. *F*, summary of *R* values of WT and rP2X4 mutants. n = 15, 7, 8, 7, 7, 5, 5, 6, and 5, from *left* to *right*, respectively. One-way ANOVA with Bonferroni post-test ($F(8, 56) = 19.98$, $p < 0.0001$). The data on WT and E118A are the same as those displayed for Figure 5*E*. *G*, concentration–response curves of ATP in rP2X4^{WT}, rP2X4^{E118A}, rP2X4$^{S141A/S142A}$, and rP2X4$^{E118A/S141A/S142A}$. The *solid lines* are fitted by Hill equation (mean ± SEM, n = 3–5, EC_{50} = 51.5 ± 16.1 and 59.6 ± 13.2 μM, n_H = 0.92 ± 0.14 and 1.07 ± 0.14 for S141A/S142A and S141A/S142A/E118A, respectively). The data of rP2X4^{WT} and rP2X4^{E118A} are the same as those displayed for Figure 4*B* and are shown here as controls. *H*, double-mutant cycle analysis between E118 and S141/S142. rP2X4, rat (*Rattus norvegicus*) P2X4.

$\Delta\Delta G$ of E118 and H140 was calculated to be −1.02 kcal/mol (Fig. 7*G*), indicating that H140 and E118 are interdependent in contributing to ATP recognition and channel gating of P2X4.

In other P2X subtypes, there is no correlation between the highly conserved residue and ATP recognition

Finally, we explored why this conserved residue has no effect on the apparent ATP affinity of other P2X subtypes (Fig. 8) by using MD simulations. In 0.5-μs MD simulations of hP2X3^{WT} or hP2X3^{E109A} at the open state, P128, the residue corresponding to H140 of rP2X4, remained away from ATP ranging from 8.4 to 14 Å (the distance between the C_α of P128 and N9 atom of ATP; Fig. 8, *A*–*C*). Although the P128 moved closer to ATP in hP2X3^{E109A}, it is still impossible to establish a direct contact between the beak region and ATP at this distance (Fig. 8, *A* and *C*). Thus, sequence differences in the beak region and/or the structure of this region in hP2X3 might compromise the role of E109 in the apparent ATP affinity of hP2X3. Similarly, MD simulations of AmP2X and AmP2X^{E129A} reveal ∼8 Å distance between the beak region and ATP (Fig. 8, *D*–*F*). Therefore, it is possible that sequence differences of the beak regions in other P2X subtypes interrupt the coupling of this conserved residue, like E118 in rP2X4, to the final ATP recognition of the P2X receptor.

Discussion

In RSSF studies, highly conserved residues often thought to have a conserved role in protein architecture and function. In our study, E121 (zfP2X4 numbering) is a highly conserved residue, but its side-chain orientation differs from that of other P2X subtypes. Accordingly, the zfP2X4^{E121A} mutant significantly altered the apparent affinity of ATP rather than the corresponding mutants in other P2X subtypes. The specific role of this unique side-chain orientation–determined conserved residue in ATP recognition is due to the coupling established by this conserved residue and adjacent nonconserved residues to the ATP recognition of P2X4. Our findings suggest that a highly conserved residue in the primary amino acid sequence could "own" the nonconserved role in proteins, and that the conserved residue is able to establish a special function with adjacent nonconserved residues.

The ability of rP2X4^{E118} in determining the ATP recognition and/or channel gating is possibly through the "E118 … S141/S142 … H 140 axis," especially for the H-bond contact between E118 and S141/S142 complexes. The following evidence can support this idea. First, several E118 mutants suggest that the strong polarity and proper side-chain size of this residue are important (Fig. 4), and stable H-bond contacts between E118 and S141/S142 could be detected during MD

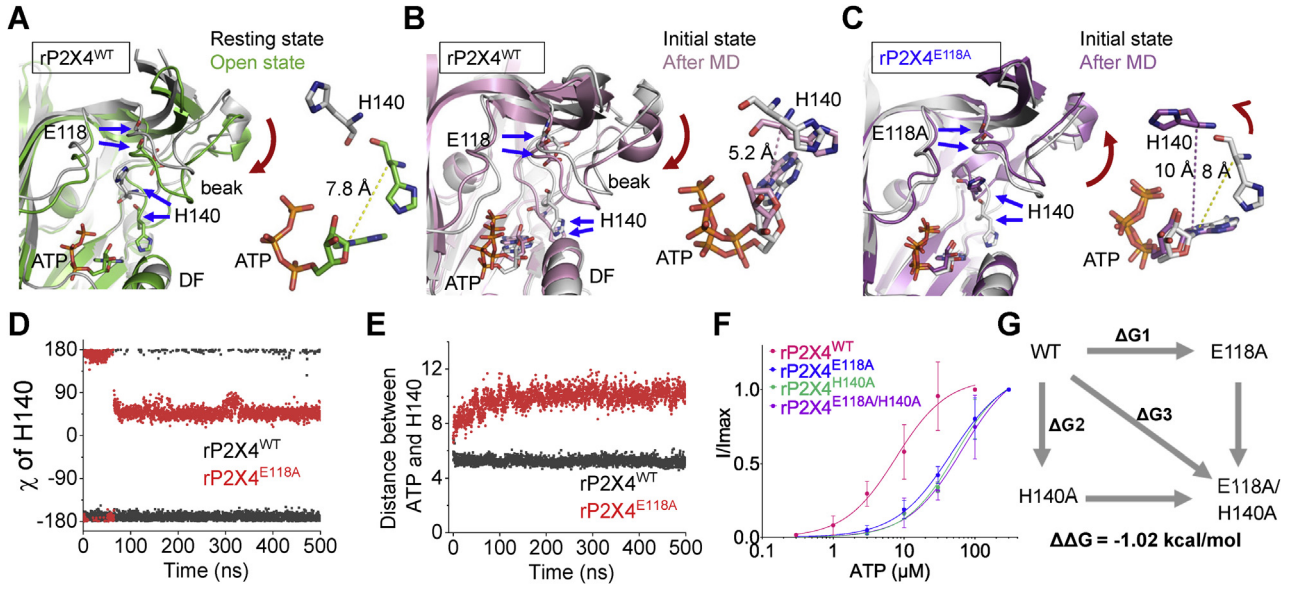

Figure 7. H140 mediates the coupling of E118 to the ATP recognition of rP2X4. *A*, superimposed apo and open structures of rP2X4 to show the downward motions of the head domain and beak region, as well as the H140s moving closing to the bound ATP. *Arrows* highlight bound ATP–induced allostery. The *yellow-dashed line* indicates the distance between the C_α of H140 and N9 atom of ATP. *B* and *C*, superimposition of the initial open structure and averaged conformations of rP2X4^{WT} (*B*) and rP2X4^{E118A} (*C*) after 0.5-μs molecular dynamics (MD) simulations. *Red arrows* indicate the conformational changes during MD simulations. *D* and *E*, fluctuations of the dihedral angle of H140 (*D*) and distance between ATP and H140 (*E*) during 0.5-μs MD simulations of rP2X4^{WT} and rP2X4^{E118A}. The trajectories were sampled every 200 ps. *F*, the ATP concentration–response curves of rP2X4^{WT}, rP2X4^{E118A}, rP2X4^{H140A}, and rP2X4$^{E118A/H140A}$ (mean ± SEM, n = 3–5, EC_{50} = 53.3 ± 9.1 and 55.1 ± 14.4 μM, n_H = 1.24 ± 0.16 and 0.99 ± 0.15 for H140A and E118A/H140A, respectively). The data on rP2X4^{WT} and rP2X4^{E118A} are the same as those displayed for Figure 4*B*. *G*, double-mutant cycle analysis between E118 and H140A. rP2X4, rat (*Rattus norvegicus*) P2X4.

simulations (Fig. 6*D*). Second, the carboxyl group of E118 is oriented toward S141/S142 at the open state, which would facilitate the H-bond contacts among these residues (Fig. 6*C*). Third, the *R* values of S141A or S142A are slightly higher than that of rP2X4 WT, but the *R* value of double-mutant S141A/S142A increases to a level equal to that of E118A, suggesting that both S141 and S142 can make contacts with E118 (Fig. 6*F*). This idea is further confirmed by the double-mutant analysis of E118 and S141/S142 (Fig. 6*H*). Fourth, during MD simulations of rP2X4^{E118A}, loss of E118 … S141/S142 contact was associated with upward movement of the beak region, which resulted in the displacement of H140 from the ATP

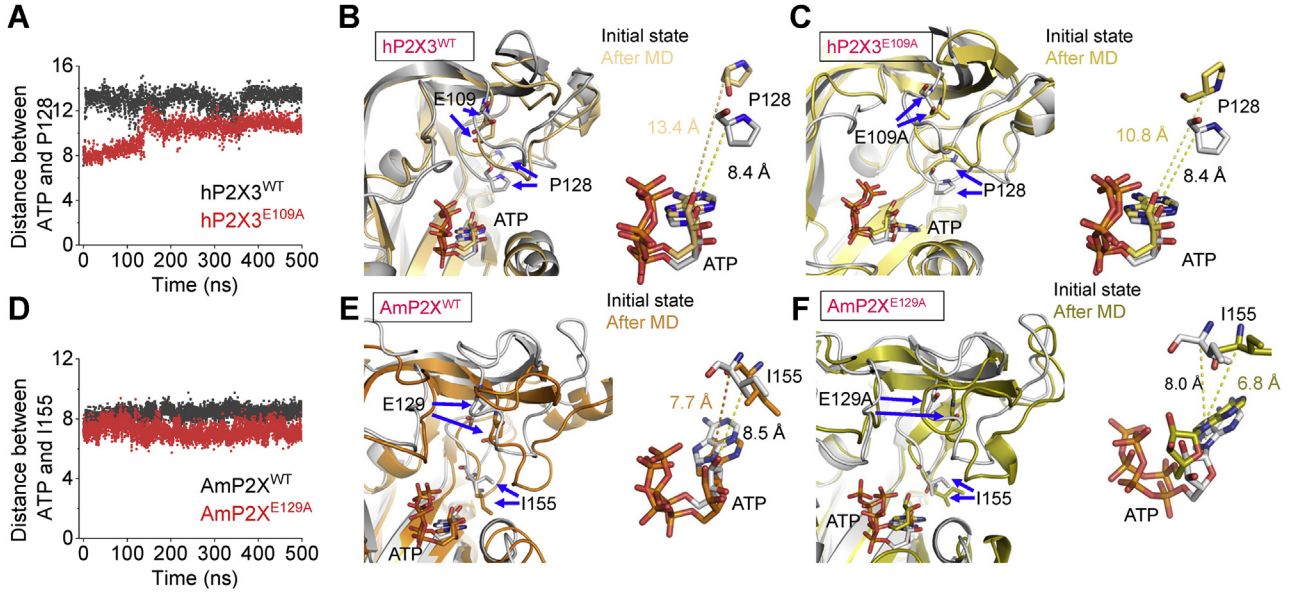

Figure 8. Molecular dynamics (MD) simulations of hP2X3^{WT}, AmP2X^{WT}, and their equivalent mutants. *A*, distance measurements between ATP and P128 during 0.5-μs MD simulations of hP2X3^{WT} and hP2X3^{E109A}. *B* and *C*, superimpositions of initial open structure and conformations after MD simulations of hP2X3^{WT} and hP2X3^{E109A}. The *dashed lines* indicate the distance between the C_α of P128 and N9 atoms of ATP. *D*, distance measurements between ATP and I115 during 0.5-μs MD simulations of AmP2X^{WT} and AmP2X^{E129A}. *E* and *F*, superimpositions of initial open structure and snapshots after MD simulations of AmP2X^{WT} and AmP2X^{E129A}. The trajectories were sampled every 200 ps. AmP2X, gulf coast tick (*Amblyomma maculatum*) P2X; hP2X3, human (*Homo sapiens*) P2X3.

(Fig. 7*C*). Double-mutant cycle analysis of E118 and H140 ($\Delta\Delta G$ = −1.02 kcal/mol) also demonstrated the functional coupling of these two residues (Fig. 7*G*). Thus, the established "E118 … S141/S142 … H140 axis" is the mechanism for the special role of E118 in determining the ATP recognition.

Our findings also support the idea that the nonconserved residue is able to significantly alter the conformation and function of highly conserved residues, especially when these conserved residues are located in a loop region. Based on the sequence alignment, we could find that although zfP2X4^{E121} is highly conserved but the other residues in the beak region (a loop structure; Fig. 1*C*) are nonconserved throughout the P2X family. Accordingly, in the crystal structure of zfP2X4, the side chain of E121 points outside the head domain, showing an extended conformation with its carboxyl group facing to the lower beak region. However, in other P2X subtypes, the side chain of the equivalent residue bends inward to the head domain, making no contact with the lower beak region. Interestingly, differences in the beak region sequences of zfP2X4 and rP2X4, from the same subtype but different species, persist, which result in different changes in their EC_{50} values under alanine substitutions in E118 and E121, respectively. However, the mere swap of the beak region failed to restore the change induced by E118A based on the rP2X4$^{zf\text{-}beak}$. It is possible that rP2X4$^{zf\text{-}beak}$ adopts a different conformation that decouples the link between E118 and the ATP-binding site. What is the physiological function of this "designed" special role of E118/E121 in the evolution of P2X4 receptors that should be further studied. We speculate that the unique role of E118/E121 in P2X4 receptors provides a different way for endogenous modulation in certain species. For example, previous studies have shown that some trace elements could regulate the function of P2X4, and that E118, H140, and their adjacent amino acids are likely to be involved in metal binding (44).

Finally, our study provides a prerequisite for the further development of new high-selective small molecule targeting P2X receptors. The upper lumen, formed by the head domains and the beak region, is an allosteric site, and several compounds/metal ions have been shown to stimulate this site (45–47). Understanding the relationship between the side-chain orientation of E118 within this site and the ATP-recognition P2X receptors will facilitate the design and optimization of potent and highly selective new analogs based on the known compounds. Furthermore, there is no compound that has been shown to act directly on the P2X4 receptor at this site, and we can screen for new P2X4-selective lead compounds.

Experimental procedures

Cell culture and mutagenesis

Human embryonic kidney 293 (HEK293) cells were cultured in 5% CO_2/95% air at 37°C in Dulbecco's modified Eagle's medium (Corning) supplemented with 10% fetal bovine serum (PAN), 1% Penicillin-Streptomycin (Gibco), and 1% Glutamax (Gibco). Calcium phosphate transfection was used for delivering plasmid DNA into HEK293 cells cultured on the coverslips placed in the 35-mm dishes. About 2.5 μg plasmid DNA was mixed directly with 100 μl 0.25 M $CaCl_2$ solution, and then, the mixed solution was slowly added into 2× Hepes-buffered saline solution with tip agitating to ensure the formation of fine calcium phosphate–DNA precipitate. Hepes-buffered saline solution (2×) contains (in millimolar) 140 NaCl, 1.5 Na_2HPO_4, 50 Hepes, and the pH was adjusted to 6.96. All mutants were constructed by KOD-Plus mutagenesis kit (Toyobo) and confirmed by DNA sequencing (Beijing Genomics Institute). rP2X4 and zfP2X4 plasmids were a gift from Drs Alan North and Lin-Hua Jiang, and AmP2X plasmid was a generous gift from Dr Motoyuki Hattori; the complementary DNAs of hP2X1 and hP2X7 were synthesized and subcloned into pcDNA3.1 by Shanghai Genechem; complementary DNAs for hP2X2, ckP2X7, and pdP2X7 were synthesized and subcloned to pcDNA3.0 by Beijing Genomics Institute; the plasmid for hP2X3 was purchased from Open Biosystems.

Electrophysiological recordings

Whole-cell patch clamp recordings were performed at room temperature (25 ± 2°C), using an Axopatch 200B amplifier (Molecular Devices). Current signals were sampled at 10 kHz and filtered at 2 kHz and analyzed by pClamp 10 (Molecular Devices). HEK293 cells were superfused with standard extracellular solution containing (in millimolar) 150 NaCl, 5 KCl, 10 glucose, 10 Hepes, 2 $CaCl_2$, and 1 $MgCl_2$ (pH 7.4). The pipettes were pulled from glass capillaries through two-stage puller (Narishige PC-10) and filled in a general intracellular solution containing (in millimolar) 120 KCl, 30 NaCl, 0.5 $CaCl_2$, 1 $MgCl_2$, 10 Hepes, 5 EGTA (pH 7.2), and a resistance varied between 2 and 4 MΩ. During gap-free recordings, the membrane potential was held at −60 mV, and the ATP solution was applied with the Y-tube. As we previously described (19, 48), nystatin-perforated patch clamp was carried out to reduce the dialysis of intracellular constituents and current rundown. Nystatin-perforated intracellular solution contains (in millimolar) 75 K_2SO_4, 55 KCl, 5 $MgSO_4$, and 10 Hepes (pH 7.2). Nystatin was purchased from Sangon Biotech, and all other drugs were purchased from Sigma–Aldrich. Maximal currents or *R* ratios were obtained by whole-cell patching, whereas concentration–response curve recordings were performed using perforated patch clamp to avoid channel desensitization.

Homology modeling and MD simulations

The homology models of rP2X4^{WT} and rP2X4^{E118A} were constructed based on the crystal structures of zfP2X4 (PDB IDs: 4DW0 and 4DW1) by using Modeler as we described previously (42, 49). The alignment of the target sequences was manually adjusted to match published alignments (13); the obtained model was checked and validated by ProCheck (50); the energy-minimized structures of P2X were used as the initial structures for MD simulations. A large 1-palmitoyl-2-oleoyl-sn-glycero-3-phosphocholine bilayer, available in System Builder of DESMOND (Schrödinger) (51), was used to generate a suitable membrane system in which the transmembrane domain of the P2X could be embedded. The P2X/

1-palmitoyl-2-oleoyl-sn-glycero-3-phosphocholine system was dissolved in simple point charge water molecules. Counter ions were then added to compensate for the net negative charge of the system. NaCl (150 mM) was added into the simulation box that represents background salt at physiological condition. The default relaxation protocol of DESMOND for each system was applied before the simulations were run: (1) 100 ps simulations in the canonical (constant moles, volume and temperature) ensemble with Brownian dynamics using a temperature of 10 K with solute heavy atoms restrained; (2) 12 ps simulations in the canonical (constant moles, volume and temperature) ensemble using Berendsen thermostat at 10 K with small-time step and solute heavy atoms restrained; (3) 12 ps simulations in the isothermal-isobaric (constant moles, pressure and temperature) ensemble using the Berendsen thermostat and barostat at 10 K and 1 atm with solute heavy atoms restrained; (4) 12 ps simulations in the isothermal-isobaric (constant moles, pressure and temperature) ensemble using the Berendsen thermostat and barostat at 300 K and 1 atm with solute heavy atoms restrained; (5) 24 ps simulations in the isothermal-isobaric (constant moles, pressure and temperature) ensemble using the Berendsen thermostat and barostat at 300 K and 1 atm with no restraints. After equilibration, the MD simulations were performed for 500 ns. Long-range electrostatic interactions were computed using the smooth particle mesh Ewald method. The integration time step used was 1 fs, and the coordinate trajectories were saved every 200 ps. All simulations were performed by using DESMOND with a constant number of particles, pressure (1 bar), and temperature (300 K) and periodic boundary conditions by using Nose–Hoover chain thermostat. Proteins, ions, lipids, and the simple point charge waters were assigned to all-atom OPLS_2005 force field (52, 53). Simulations were run on DELL T7910 graphic working station (with NVIDA Tesla K40C-GPU). Preparation, analysis, and visualization were performed on a 12-CPU CORE DELL T7500 graphic working station.

Data analysis

Bonferroni's multiple comparisons test (ANOVA) was used when there were more than two groups. $^{*}p < 0.05$ or $^{**}p < 0.01$ was considered significant. Concentration–response curves were fitted to the equation as $I/I_{max} = 1/(1 + (EC_{50}/[ATP])^{n})$, where I is the normalized current at a given concentration of ATP, I_{max} is the maximum normalized current, EC_{50} is ATP dose for half-maximal effect, and n is the Hill coefficient. Statistical comparison between EC_{50} values was performed using extra sum-of-squares F tests. The change in Gibbs free energy upon each mutant was described by the following equation: $\Delta G = -RT \ln\left(\frac{EC_{50}\text{ of WT}}{EC_{50}\text{ of mut}}\right)$, where the constants R and T are 1.987 cal/mol/K and 293 K, respectively (54). The interaction free energy in the double-mutant cycles was calculated from $\Delta\Delta G_{interaction} = \Delta G_{mut1+2} - (\Delta G_{mut1} + \Delta G_{mut2})$. If the change in the free energy of the double mutant (ΔG_{mut1+2}) equals the sum of the free energy changes of the corresponding single mutations (ΔG_{mut1} and ΔG_{mut2}), which means that the value of $\Delta\Delta G_{interaction}$ is close to zero, the two residues or clusters will not interact. In contrast, if the two residues interact, the change in the free energy of the double mutant will differ from the sum of the changes of the corresponding single mutations, and $\Delta\Delta G_{interaction}$ should be larger than ±0.35 kcal/mol (37) that has been reported for noninteracting residues.

Data availability

All data are contained within the article.

Author contributions—Y. Y. initiated the project. Y. Y. and J. W. designed research. P.-F. C., X.-F. M., L.-F. S., Y. T., Y.-Z. F., P. L., Z. X., and J. W. performed researches. P.-F. C., M. X. Z., C. L., C.-R. G., J. W., and Y. Y. analyzed data. P.-F. C., J. W., M. X. Z., and Y. Y. wrote the article. All authors discussed the results and commented on the article.

Funding and additional information—This study was supported with funds from the National Natural Science Foundation of China with grant number 32000869 (J. W.), 31570832 (Y. Y.), 31971146 (Y. Y.), 81603409 (Y.-Z. F.), and 31971042 (Y. T.), Natural Science Foundation of Jiangsu Province (BK20202002 to Y. Y.), Innovation and Entrepreneurship Talent Program of Jiangsu Province (Y. Y. and J. W.), Open Project of State Key Laboratory of Natural Medicines (SKLNMZZRC201801 to Y. Y.), Hunan Provincial Natural Science Foundation of China (2018JJ1012 to Y. T.), Guangxi Funds for Distinguished Experts (Y. Y.), and State Key Laboratory of Utilization of Woody Oil Resource with grant number 2019XK2002 (C. L.).

Conflict of interest—The authors declare that they have no conflicts of interest with the contents of this article.

Abbreviations—The abbreviations used are: AmP2X, gulf coast tick (*Amblyomma maculatum*) P2X; ckP2X7, chicken (*Gallus gallus domesticus*) P2X7; HEK293, human embryonic kidney 293; hP2X3, human (*Homo sapiens*) P2X3; MD, molecular dynamics; PDB, Protein Data Bank; pdP2X7, giant panda (*Ailuropoda melanoleuca*) P2X7; rP2X7, rat (*Rattus norvegicus*) P2X7; RSSF, relationship between sequence, structure, and function; zfP2X4, zebrafish (*Danio rerio*) P2X4.

References

1. Zavodszky, M. I., and Kuhn, L. A. (2005) Side-chain flexibility in protein-ligand binding: The minimal rotation hypothesis. *Protein Sci.* **14**, 1104–1114
2. Tanaka, D., Nagashima, Y., Hara, M., Nagano, S., and Seki, T. (2015) Alternation of side-chain mesogen orientation caused by the backbone structure in liquid-crystalline polymer thin films. *Langmuir* **31**, 11379–11383
3. Alapati, R., Shuvo, M. H., and Bhattacharya, D. (2020) SPECS: Integration of side-chain orientation and global distance-based measures for improved evaluation of protein structural models. *PLoS One* **15**, e0228245
4. Wieman, H., Tondel, K., Anderssen, E., and Drablos, F. (2004) Homology-based modelling of targets for rational drug design. *Mini Rev. Med. Chem.* **4**, 793–804

5. Zhao, J., Cao, Y., and Zhang, L. (2020) Exploring the computational methods for protein-ligand binding site prediction. *Comput. Struct. Biotechnol. J.* **18**, 417–426
6. Capra, J. A., and Singh, M. (2007) Predicting functionally important residues from sequence conservation. *Bioinformatics* **23**, 1875–1882
7. Ranganathan, S., Nakai, K., and Schönbach, C. (2019) *Encyclopedia of Bioinformatics and Computational Biology: ABC of Bioinformatics*
8. Taujale, R., Venkat, A., Huang, L. C., Zhou, Z., Yeung, W., Rasheed, K. M., Li, S., Edison, A. S., Moremen, K. W., and Kannan, N. (2020) Deep evolutionary analysis reveals the design principles of fold A glycosyltransferases. *Elife* **9**, e54532
9. VernonBryson, and Vogel, H. (1965) *Evolving Genes and Proteins*, Academic Press, New York
10. van Goor, M. K., de Jager, L., Cheng, Y., and van der Wijst, J. (2020) High-resolution structures of transient receptor potential vanilloid channels: Unveiling a functionally diverse group of ion channels. *Protein Sci.* **29**, 1569–1580
11. Wang, J., Hua, T., and Liu, Z. J. (2020) Structural features of activated GPCR signaling complexes. *Curr. Opin. Struct. Biol.* **63**, 82–89
12. Huang, Y., Fliegert, R., Guse, A. H., Lu, W., and Du, J. (2020) A structural overview of the ion channels of the TRPM family. *Cell Calcium* **85**, 102111
13. Kawate, T., Michel, J. C., Birdsong, W. T., and Gouaux, E. (2009) Crystal structure of the ATP-gated P2X(4) ion channel in the closed state. *Nature* **460**, 592–598
14. Hattori, M., and Gouaux, E. (2012) Molecular mechanism of ATP binding and ion channel activation in P2X receptors. *Nature* **485**, 207–212
15. Kasuya, G., Fujiwara, Y., Tsukamoto, H., Morinaga, S., Ryu, S., Touhara, K., Ishitani, R., Furutani, Y., Hattori, M., and Nureki, O. (2017) Structural insights into the nucleotide base specificity of P2X receptors. *Sci. Rep.* **7**, 45208
16. Kasuya, G., Fujiwara, Y., Takemoto, M., Dohmae, N., Nakada-Nakura, Y., Ishitani, R., Hattori, M., and Nureki, O. (2016) Structural insights into divalent cation modulations of ATP-gated P2X receptor channels. *Cell Rep.* **14**, 932–944
17. Kasuya, G., Yamaura, T., Ma, X. B., Nakamura, R., Takemoto, M., Nagumo, H., Tanaka, E., Dohmae, N., Nakane, T., Yu, Y., Ishitani, R., Matsuzaki, O., Hattori, M., and Nureki, O. (2017) Structural insights into the competitive inhibition of the ATP-gated P2X receptor channel. *Nat. Commun.* **8**, 876
18. Mansoor, S. E., Lu, W., Oosterheert, W., Shekhar, M., Tajkhorshid, E., and Gouaux, E. (2016) X-ray structures define human P2X(3) receptor gating cycle and antagonist action. *Nature* **538**, 66–71
19. Wang, J., Wang, Y., Cui, W. W., Huang, Y., Yang, Y., Liu, Y., Zhao, W. S., Cheng, X. Y., Sun, W. S., Cao, P., Zhu, M. X., Wang, R., Hattori, M., and Yu, Y. (2018) Druggable negative allosteric site of P2X3 receptors. *Proc. Natl. Acad. Sci. U. S. A.* **115**, 4939–4944
20. McCarthy, A. E., Yoshioka, C., and Mansoor, S. E. (2019) Full-length P2X7 structures reveal how palmitoylation prevents channel desensitization. *Cell* **179**, 659–670.e613
21. Karasawa, A., and Kawate, T. (2016) Structural basis for subtype-specific inhibition of the P2X7 receptor. *Elife* **5**, e22153
22. Coddou, C., Yan, Z., Obsil, T., Huidobro-Toro, J. P., and Stojilkovic, S. S. (2011) Activation and regulation of purinergic P2X receptor channels. *Pharmacol. Rev.* **63**, 641–683
23. Burnstock, G. (2008) Purinergic signalling and disorders of the central nervous system. *Nat. Rev. Drug Discov.* **7**, 575–590
24. Bele, T., and Fabbretti, E. (2015) P2X receptors, sensory neurons and pain. *Curr. Med. Chem.* **22**, 845–850
25. Bernier, L. P., Ase, A. R., and Seguela, P. (2018) P2X receptor channels in chronic pain pathways. *Br. J. Pharmacol.* **175**, 2219–2230
26. Franceschini, A., and Adinolfi, E. (2014) P2X receptors: New players in cancer pain. *World J. Biol. Chem.* **5**, 429–436
27. Yamamoto, K., Sokabe, T., Matsumoto, T., Yoshimura, K., Shibata, M., Ohura, N., Fukuda, T., Sato, T., Sekine, K., Kato, S., Isshiki, M., Fujita, T., Kobayashi, M., Kawamura, K., Masuda, H., *et al.* (2006) Impaired flow-dependent control of vascular tone and remodeling in P2X4-deficient mice. *Nat. Med.* **12**, 133–137
28. Eltzschig, H. K., Sitkovsky, M. V., and Robson, S. C. (2013) Purinergic signaling during inflammation. *N. Engl. J. Med.* **368**, 1260
29. Burnstock, G., and Kennedy, C. (2011) P2X receptors in health and disease. *Adv. Pharmacol.* **61**, 333–372
30. Hechler, B., and Gachet, C. (2015) Purinergic receptors in thrombosis and inflammation. *Arterioscler. Thromb. Vasc. Biol.* **35**, 2307–2315
31. Khakh, B. S., and North, R. A. (2006) P2X receptors as cell-surface ATP sensors in health and disease. *Nature* **442**, 527–532
32. Vial, C., Roberts, J. A., and Evans, R. J. (2004) Molecular properties of ATP-gated P2X receptor ion channels. *Trends Pharmacol. Sci.* **25**, 487–493
33. North, R. A. (2002) Molecular physiology of P2X receptors. *Physiol. Rev.* **82**, 1013–1067
34. Newbolt, A., Stoop, R., Virginio, C., Surprenant, A., North, R. A., Buell, G., and Rassendren, F. (1998) Membrane topology of an ATP-gated ion channel (P2X receptor). *J. Biol. Chem.* **273**, 15177–15182
35. Jiang, L. H., Rassendren, F., Surprenant, A., and North, R. A. (2000) Identification of amino acid residues contributing to the ATP-binding site of a purinergic P2X receptor. *J. Biol. Chem.* **275**, 34190–34196
36. Li, M., Silberberg, S. D., and Swartz, K. J. (2013) Subtype-specific control of P2X receptor channel signaling by ATP and Mg2+. *Proc. Natl. Acad. Sci. U. S. A.* **110**, E3455–E3463
37. Schreiber, G., and Fersht, A. R. (1995) Energetics of protein-protein interactions: Analysis of the Barnase-Barstar interface by single mutations and double mutant cycles. *J. Mol. Biol.* **248**, 478–486
38. Pierdominici-Sottile, G., Moffatt, L., and Palma, J. (2016) The dynamic behavior of the P2X4 ion channel in the closed conformation. *Biophys. J.* **111**, 2642–2650
39. Kawate, T. (2017) P2X receptor activation. *Adv. Exp. Med. Biol.* **1051**, 55–69
40. Kowalski, M., Hausmann, R., Dopychai, A., Grohmann, M., Franke, H., Nieber, K., Schmalzing, G., Illes, P., and Riedel, T. (2014) Conformational flexibility of the agonist binding jaw of the human P2X3 receptor is a prerequisite for channel opening. *Br. J. Pharmacol.* **171**, 5093–5112
41. Huang, L. D., Fan, Y. Z., Tian, Y., Yang, Y., Liu, Y., Wang, J., Zhao, W. S., Zhou, W. C., Cheng, X. Y., Cao, P., Lu, X. Y., and Yu, Y. (2014) Inherent dynamics of head domain correlates with ATP-recognition of P2X4 receptors: Insights gained from molecular simulations. *PLoS One* **9**, e97528
42. Zhao, W. S., Wang, J., Ma, X. J., Yang, Y., Liu, Y., Huang, L. D., Fan, Y. Z., Cheng, X. Y., Chen, H. Z., Wang, R., and Yu, Y. (2014) Relative motions between left flipper and dorsal fin domains favour P2X4 receptor activation. *Nat. Commun.* **5**, 4189
43. Jiang, R., Taly, A., Lemoine, D., Martz, A., Cunrath, O., and Grutter, T. (2012) Tightening of the ATP-binding sites induces the opening of P2X receptor channels. *EMBO J.* **31**, 2134–2143
44. Igawa, T., Abe, Y., Tsuda, M., Inoue, K., and Ueda, T. (2015) Solution structure of the rat P2X4 receptor head domain involved in inhibitory metal binding. *FEBS Lett.* **589**, 680–686
45. Wang, J., and Yu, Y. (2016) Insights into the channel gating of P2X receptors from structures, dynamics and small molecules. *Acta Pharmacol. Sin.* **37**, 44–55
46. North, R. A., and Jarvis, M. F. (2013) P2X receptors as drug targets. *Mol. Pharmacol.* **83**, 759–769
47. Coddou, C., Stojilkovic, S. S., and Huidobro-Toro, J. P. (2011) Allosteric modulation of ATP-gated P2X receptor channels. *Rev. Neurosci.* **22**, 335–354
48. Li, B., Wang, J., Cheng, X. Y., Liu, Y., Yang, Y., Yang, X. N., Guo, C. R., Niu, Y. Y., Cao, P., Lu, X. Y., Zhu, M. X., Tian, Y., and Yu, Y. (2018) Molecular mechanism underlying the subtype-selectivity of competitive inhibitor NF110 and its distinct potencies in human and rat P2X3 receptors. *Sci. Bull.* **63**, 1616–1625

49. Wang, J., Sun, L. F., Cui, W. W., Zhao, W. S., Ma, X. F., Li, B., Liu, Y., Yang, Y., Hu, Y. M., Huang, L. D., Cheng, X. Y., Li, L., Lu, X. Y., Tian, Y., and Yu, Y. (2017) Intersubunit physical couplings fostered by the left flipper domain facilitate channel opening of P2X4 receptors. *J. Biol. Chem.* **292**, 7619–7635
50. Laskowski, R. A., Macarthur, M. W., Moss, D. S., and Thornton, J. M. (1993) Procheck - a program to check the stereochemical quality of protein structures. *J. Appl. Crystallogr.* **26**, 283–291
51. Shaw, D. E. (2005) A fast, scalable method for the parallel evaluation of distance-limited pairwise particle interactions. *J. Comput. Chem.* **26**, 1318–1328
52. Kaminski, G. A., Friesner, R. A., Tirado-Rives, J., and Jorgensen, W. L. (2001) Evaluation and reparametrization of the OPLS-AA force field for proteins via comparison with accurate quantum chemical calculations on peptides. *J. Phys. Chem. B* **105**, 6474–6487
53. Jorgensen, W. L., Maxwell, D. S., and TiradoRives, J. (1996) Development and testing of the OPLS all-atom force field on conformational energetics and properties of organic liquids. *J. Am. Chem. Soc.* **118**, 11225–11236
54. Hausmann, R., Gunther, J., Kless, A., Kuhlmann, D., Kassack, M. U., Bahrenberg, G., Markwardt, F., and Schmalzing, G. (2013) Salt bridge switching from Arg290/Glu167 to Arg290/ATP promotes the closed-to-open transition of the P2X2 receptor. *Mol. Pharmacol.* **83**, 73–84